HHS Public Access

Author manuscript

Cell Metab. Author manuscript; available in PMC 2020 March 05.

Published in final edited form as:

Cell Metab. 2019 March 05; 29(3): 736–744.e7. doi:10.1016/j.cmet.2018.12.022.

Oxyphor 2P: A High-Performance Probe for Deep-Tissue Longitudinal Oxygen Imaging

Tatiana V. Esipova[1,5], **Matthew J. P. Barrett**[3,5], **Eva Erlebach**[3], **Artëm E. Masunov**[4], **Bruno Weber**[3], and **Sergei A. Vinogradov**[1,2,6]

[1]Department of Biochemistry and Biophysics, Perelman School of Medicine, University of Pennsylvania, Philadelphia, PA 19104, USA. [2]Department of Chemistry, School of Arts and Sciences, University of Pennsylvania, Philadelphia, PA 19104, USA. [3]Institute of Pharmacology and Toxicology, University of Zurich, and Neuroscience Center Zurich, Zurich CH-8057, Switzerland. [4]NanoScience Technology Center, Department of Chemistry and School of Modeling, Simulation and Training, University of Central Florida, Orlando, FL 32826, USA; National Research Nuclear University MEPhI, Kashirskoye Shosse 31, Moscow 115409, Russia; South Ural State University, Lenin Pr. 76, Chelyabinsk 454080, Russia. [5]These authors contributed equally to this work. [6]Lead contact.

SUMMARY

Quantitative imaging of oxygen distributions in tissue can provide invaluable information about metabolism in normal and diseased states. Two-Photon Phosphorescence Lifetime Microscopy (2PLM) has been developed to perform measurements of oxygen *in vivo* with micron-scale resolution in 3D; however, the method's potential has not yet been fully realized due to the limitations of current phosphorescent probes technology. Here we report a new sensor, Oxyphor 2P, which enables oxygen microscopy twice as deep (up to 600 μm below the tissue surface) and with ~60 times higher speed than previously possible. Oxyphor 2P allows longitudinal oxygen measurements without having to inject the probe directly into the imaged region. As proof-of-principle, we monitored oxygen dynamics for days following micro-stroke induced by occlusion of a single capillary in the mouse brain. Oxyphor 2P opens up new possibilities for studies of tissue metabolic states using 2PLM in a wide range of biomedical research areas.

Correspondence: vinograd.upenn@gmail.com, bweber@pharma.uzh.ch.

AUTHOR CONTRIBUTIONS

S.A.V. and B.W. conceived the project. T.V.E performed organic synthesis and photophysical characterization. M.J.P.B. and E.E. performed biological microscopy experiments and data analysis. A.E.M. performed quantum chemistry calculations. S.A.V performed non-linear spectroscopy experiments and probe calibrations. S.A.V and B.W. directed the project. T.V.E., M.J.P.B and S.A.V. wrote the paper with input from all other authors.

SUPPLEMENTAL INFORMATION

Supplemental Information includes one file (pdf).

Declaration of Interest

S.A.V. has partial ownership of Oxygen Enterprises Ltd, which owns the intellectual property for dendritic phosphorescent oxygen probes technology (US Pat. No. 9,556,213; US 2017/0137449 A1).

eTOC blurb

Two-photon phosphorescence lifetime microscopy (2PLM) allows dynamic imaging of oxygen distributions in living tissue in 3D. Esipova et al. developed a new probe for 2PLM, Oxyphor 2P, that greatly improves over the existing technology, allowing for imaging twice as deep (up to 600μm) with ~60 times higher temporal resolution and accuracy.

Keywords

oxygen imaging; two-photon microscopy; phosphorescence; porphyrin; dendrimer; stroke

INTRODUCTION

Molecular oxygen plays a unique role in cellular energy metabolism by serving as the terminal electron acceptor in the mitochondrial respiratory chain. Consumption of oxygen is tightly coupled to the production of cellular energy, while physiological levels of partial pressures of oxygen (pO_2) vary considerably depending on the tissue type and metabolic load (Erecinska and Silver, 2001; Tsai et al., 2003). Low pO_2 levels ultimately cause decrease in the cellular energy state (Wilson, 2015), triggering a vast transcriptional cascade regulating multiple genes (Ratcliffe, 2013) and in many cases indicating onset of pathology. However, quantitative links between oxygen levels and tissue pathologic states are still poorly understood in part because of technical challenges associated with quantification of endogenous molecules and metabolites *in vivo*. To this end, methods for dynamic imaging of oxygen in tissues with high spatial and temporal resolution are invaluable for many areas of biomedical research, including biology of cancer (Ratcliffe, 2013), hypoxic ischemic injury in stroke (Ham and Raju, 2017), macular degeneration (Kurihara et al., 2016) as well as for fundamental studies of tissue metabolism.

In its ground electronic state oxygen molecule has triplet spin multiplicity. This property has major implications for all nature's oxygen-involving reactions, but it also provides an opportunity to optically measure oxygen concentrations in tissue. Rapidly diffusing oxygen molecules quench emission originating from triplet states of other molecular species, known as phosphorescence. If a phosphorescent dye (below referred to as a *probe*) is dissolved in a biological medium and excited by a pulse of light, its triplet decay time, or phosphorescence lifetime, becomes a quantitative reporter of the local oxygen concentration. The related approach, known as the *phosphorescence quenching method* (Vanderkooi et al., 1987), allows minimally invasive optical quantification of oxygen *in vivo* under unperturbed physiological conditions (Rumsey et al., 1988).

Two-photon phosphorescence lifetime microscopy (2PLM) of oxygen, which is a combination of phosphorescence quenching and two-photon (2P) laser scanning microscopy, enables imaging of oxygen distributions and concentration gradients in 3D with micron-scale resolution (Finikova et al., 2008). Phosphorescence is emitted on the microsecond time-scale, i.e. 3–4 orders of magnitude slower than more commonly used fluorescence. The long lifetimes make phosphorescence exquisitely sensitive to oxygen, but subsequently limit the speed at which the lifetimes can be measured. The time needed to collect all the

phosphorescent photons after a single excitation pulse is typically in the range of hundreds of microseconds (e.g. 200–1000 μs). Depending on the number of photons that are emitted and acquired per pulse, the actual decay measurement can take from fractions of a second to many seconds. Therefore, the emission quantum yield and excitation efficiency of the probe are especially important, as they ultimately define the pixel dwell time and the ability to image oxygen dynamically.

The original probes for 2PLM (e.g. PtP-C343) were complex multichromophoric constructs built around phosphorescent metalloporphyrins (Brinas et al., 2005; Finikova et al., 2008). Porphyrins have vanishingly small two-photon absorption (2PA) cross-sections (see below), and in order to improve excitation efficiency multiple two-photon-absorbing chromophores were included in the probe molecule, forming a two-photon antenna array for capturing the excitation energy and funneling it to the porphyrin *via* intramolecular energy transfer. Both the antenna and the porphyrin were parts of the same dendritic macromolecule, whereby the dendrimer played the role of a scaffold, simultaneously helping to fine-tune oxygen sensitivity of the probe. Multiple polyethyleneglycol residues, attached to the dendrimer termini, solubilized the construct and prevented unwanted interactions of the probe with biological macromolecules. The first two-photon oxygen probes were very successful in demonstrating the method's potential, providing valuable information for neuroscience (Devor et al., 2011; Kazmi et al., 2013; Lecoq et al., 2011; Lyons et al., 2016; Parpaleix et al., 2013; Sakadzic et al., 2014; Sakadzic et al., 2010) and stem cell biology (Spencer et al., 2014). However, their complex multichromophoric structures caused a number of problems. For example, close distances between the chromophores, required for efficient energy transfer, opened up various intramolecular triplet state quenching pathways (Finikova et al., 2007), lowering probe's emissivity and degrading imaging performance. In addition, emission bands of the original probes were in the red part of the spectrum, near 650–700 nm, limiting imaging to no deeper than ~300 μm below the tissue surface (Lecoq et al., 2011). Subsequent attempts to optimize the multichromophoric design led only to moderate improvements (Roussakis et al., 2014), while approaches based on various types of nanoparticles (Choi et al., 2012; Khan et al., 2017; Lemon et al., 2015) rendered either sensors with poor oxygen sensitivity or low quantum yields, or both.

Here we report a new two-photon oxygen probe, which does not use antennae, but instead relies on a single chromophore that combines intrinsically high two-photon absorption (2PA) cross-section and unprecedentedly high phosphorescence quantum yield. The new sensor, termed Oxyphor 2P, enables oxygen imaging at speeds and depths far exceeding those accessible previously. Due to its exceptional brightness Oxyphor 2P also makes it possible to implement a new superior probe delivery method to the brain tissue extravascular space, eliminating the necessity of direct injection of the probe into the imaged area and minimizing tissue damage. As a demonstration of performance we used the new method to measure tissue oxygenation during several days following induction of a single-capillary micro-stroke, exemplifying the potential of the probe for quantitative imaging of pathological states.

RESULTS AND DISCUSSION

Probe Development

From both the synthetic and photophysical points of view, a phosphorescent sensor based on a single chromophore with optical transitions in the tissue transparency window (700–1000 nm), large two-photon absorption (2PA) cross-section and high emission quantum yield would offer many advantages compared to multichromophoric molecules. Pt or Pd porphyrins are the chromophores of choice for construction of biological oxygen probes (Quaranta et al., 2012), however their centrosymmetric structures make them highly inefficient as 2P absorbers. In centrosymmetric molecules selection rules forbid 2P transitions to one-photon (1P)-allowed *ungerade* states, such as low lying Q- and B-states in porphyrins (Fig. 1A). At the same time, 2P-active *gerade* states (*g*-states) in porphyrins lie at such high energies that their 2P excitation becomes overshadowed by 1P absorption to the low-lying singlet or even triplet states (Fig. 1A). The latter process ($T_1 \leftarrow S_0$) is strictly spin-forbidden, but in Pt and Pd porphyrins the forbiddance is partially lifted due to the very strong spin-orbit coupling (Finikova et al., 2007).

A break-through has become possible due to our recent finding that the modification of benzoporphyrins with carbonyl-containing functional groups dramatically increases 2PA near their B states (Esipova et al., 2016). Quantum chemistry calculations attributed this effect to the stabilization of *g*-states, and particularly strong stabilization was predicted for porphyrins with pyrrolic units fused with phthalimide residues, e.g. tetraarylphthalimidoporphyrins (TAPIP) (Fig. 1A). Experimental studies fully verified this prediction (Esipova et al., 2017b).

Based on the above results we chose to construct a new antenna-free probe, Oxyphor 2P, using PtTAPIP as a single chromophore (Fig. 1B). In PtTAPIP, eight carbonyl groups (shown in red) are locked in-plane with the porphyrin, ensuring high degree of conjugation and maximal stabilization of the 2P-active *g*-state. Indeed, the 2PA maximum of Oxyphor 2P is shifted even below the B-state level (λ_{max}=960 nm, Fig. 1C). Combined with a large 2PA cross-section ($\sigma^{(2)}$~650 GM) this unique feature enables efficient 2P excitation while fully avoiding overlap with the triplet vibronic sublevels. The second small 2PA maximum at 1140 nm ($\sigma^{(2)}$~30 GM, Fig. 1D) may be useful for multiplexed excitation of Oxyphor 2P along with fluorophores that do not possess 2PA in the far red regions. Having no *meso*-substituents, the macrocycle of PtTAPIP is completely planar (Supplemental Information, Fig. S1A), which is a prerequisite of high emissivity (Lebedev et al., 2008). The phosphorescence quantum yield of PtTAPIP reaches as high as 0.45 in dimethylformamide (22°C) (Esipova et al., 2017b), and decreases to 0.23 in water, which is a common trend for phosphorescent porphyrins (Finikova et al., 2008; Roussakis et al., 2014). Nevertheless, the two-photon brightness of Oxyphor 2P (i.e. the product of 2PA cross-section and emission quantum yield) exceeds that of the established probe PtP-C343 (Finikova et al., 2008) by ~60-fold. An additional advantage comes from the fact that the emission maximum of Oxyphor 2P (λ_{max}=758 nm) (Fig. 1D) is red-shifted by ~100 nm relative to that of PtP-C343 (Finikova et al., 2008), i.e. well into the tissue near infrared window. It is this feature that is responsible for a major increase in tissue depths accessible by 2PLM (see below).

Noteworthy, Oxyphor 2P also exhibits exceptionally large linear molar extinction coefficient (λ_{max} =630 nm, ε~275,000 $M^{-1}cm^{-1}$), which in combination with high emissivity makes it the brightest phosphorescent probe for oxygen sensing applications known today.

In order to protect the core of the probe from interactions with endogenous biological molecules and to simultaneously fine-tune the rate of phosphorescence quenching for optimal oxygen sensitivity we employed our earlier developed dendritic protection strategy (Lebedev et al., 2009; Vinogradov and Wilson, 2012). The phthalimide nitrogens on PtTAPIP were extended by 2,6-substituted aryl groups (Fig. 1D) to prevent intermolecular π-π stacking of otherwise completely planar structures (Supplemental Information, Fig. S1A). The linkers appended to the 2,6-positions were thus directed above and below the macrocycle plane, facilitating attachment of the bulky dendrons. The dendrimer was constructed from aryl-glycine/glutamic acid fragments and modified on the periphery with polyethyleneglycol (PEG)-amine residues (Av. MW 1000). According to molecular mechanics simulations (AMBER force field), in a folded state the probe is ~7 nm in diameter (Fig. 1C). As a result of the extensive PEGylation, Oxyphor 2P exhibits nearly unlimited aqueous solubility and shows no signs of aggregation even at concentrations >100-fold exceeding those required for imaging (typically ~5–10 μM). The phosphorescence lifetime of the probe changes from ~9 μs in air to ~38 μs under fully anaerobic conditions (36.7°C). The dependence of the calibration plot on temperature could be modeled using a 'modified' Stern-Volmer equation, $pO_2(\tau)=1/(a\times k_q\times\tau^p)+1/(k_q\times\tau_0)$, where only one parameter, k_q, is temperature-dependent (linearly), while the empirical parameters a=14.8 and p=−1.26 as well as the phosphorescence lifetime in the absence of oxygen, τ_0, are constant. The oxygen quenching plot of Oxyphor 2P in rat blood plasma is identical to that obtained using phosphate buffer saline (PBS) solution (Fig. 1E), indicating that *in vitro* calibrations (Supplemental Information) can be used directly for *in vivo* measurements. The calibrations were found to be completely insensitive to changes in pH (pH 6–9) (Fig. 1F) and to the presence of common metal ions, such Na^+, K^+, Ca^{2+}, Mg^{2+} (Supplemental Information, Fig. S1B).

It is worth mentioning that Oxyphor 2P is structurally very similar to its predecessor PtP-C343 (Finikova et al., 2008) as well as to other dendritically protected phosphorescent probes (Esipova et al., 2011). Changing a chromophore, which is embedded deep inside the dendritic shell, is unlikely to affect biological properties of a fully PEGylated macromolecule. In this regard, previous probes have shown no signs of cellular toxicity or phototoxicity neither *in vitro* (Ceroni et al., 2011) nor *in vivo* (Sakadzic et al., 2010). As expected, Oxyphor 2P showed no apparent toxicity when used either systemically or injected locally, as described below.

Benchmarking performance of Oxyphor 2P

To benchmark Oxyphor 2P against an established probe PtP-C343 we chose to perform intravascular brain oxygen measurements. In terms of the key imaging parameters (speed and depth) the comparison between probes is independent of their tissue localization (intrvascular *vs* extravascular). On the other hand, intravascular measurements are much less invasive than extravascular measurements (commonly referred to as *tissue* measurements),

since the probe can be injected far away from the measurement site (e.g. into the tail vein). Furthermore, upon intravascular injection the probe is distributed throughout the entire body, and its concentration in the measurement medium (blood plasma) is uniform, facilitating accurate comparison of the signals acquired at different imaging depths.

Imaging speed.—First we measured pO_2 changes in surface arteries and veins in the brain cerebral cortex (Fig. 2A–B) in freely-breathing, lightly-sedated mice (3 mice in total) in response to brief periods of hyperoxia and anoxia. Our two-photon microscope was optimized for 2PLM, while the sets of optical filters were chosen specifically for Oxyphor 2P or for PtP-C343 (STAR Methods). The measurements were performed using Oxyphor 2P and PtP-C343 in the same vessels, but with a delay of one week between experiments with the different probes to ensure complete clearance of one probe from the blood before injecting another. The goal was to compare the performance of the two probes at equal concentrations (~5 μM in the blood) under identical excitation regimes. In each animal we performed measurements in 12 locations with ~2Hz frequency, i.e. 12 points in ~0.5s (Fig. 2B–C; see STAR Methods for data acquisition details). The blood pO_2 increased rapidly after changing the inhaled gas from air to 100% O_2 (Fig. 2C and Supplemental Information, Fig. S2A), subsequently dropped upon switching to 100% N_2, and then returned toward the baseline after switching back to air (Fig. 2C). Above pO_2=150 mmHg the pO_2 values were obtained by extrapolation of the calibration curve and hence should be considered approximate, since the probe was calibrated only in the physiological oxygen range (0–150 mmHg).

When the data averaging period was 0.5s (per 12 locations) the baseline measured with PtP-C343 was unacceptably noisy, and the responses to the gas mixture changes were practically obscured (Fig. 2D). In contrast, with Oxyphor 2P the traces were smooth and all trends were well-detectable (Fig. 2C). For example, in the case of an artery with pO_2~103 mmHg after averaging 100 phosphorescence decays the standard error with Oxyphor 2P was ±1.8 mmHg, while for PtP-C343 it was ±18 mmHg. A comparison of the measurement errors performed for two individual vessels, an artery and a vein, in the same animal revealed that in order to reach a comparable level of accuracy, ~60 times longer acquisition was required with PtP-C343 than with Oxyphor 2P (Supplemental Information, Fig. S2B). A statistical approach using linear mixed effects models (STAR Methods) was then used to compare the measurements using the two probes across multiple animals, vessels and average baseline pO_2 values (Fig. 2E,F), since these factors affect the measurement error. The sets of the baseline pO_2 values (3 animals, 36 vessels in total) for the measurements with Oxyphor 2P and PtP-C343 covered approximately the same range and had similar distributions ($p=0.72$, Fig. 2F), indicating that comparison between the average standard errors calculated for these sets was appropriate. This comparison similarly showed that PtP-C343 requires ~60 times longer measurement than Oxyphor 2P to achieve comparable measurement accuracy (Fig. 2E).

Temporal and spatial resolution of 2PLM, probe sensitivity and measurement accuracy comprise a set of interconnected parameters. The highest possible spatial resolution is achieved when the excitation volume is diffraction-limited, potentially allowing for measurements of very fine oxygen gradients, such as those forming near a single respiring

cell. For any desired level of precision in pO_2 determination the acquisition time can be estimated by considering the probe concentration, photophysical constants, parameters of the imaging system (e.g. detector quantum efficiency, collection efficiency of the optics etc) and taking into account the relationship between the number of acquired photons and the accuracy in the measurement of the decay kinetics (Kollner and Wolfrum, 1992; Sinks et al., 2010a). In STAR Methods we provide an example of such estimate, showing that resolving pO_2 levels with accuracy of ±1mmHg at an average pO_2 level near 20mmHg, using Oxyphor 2P (10μM) at 36.6°C, requires measurements of phosphorescence lifetimes with accuracy of 1.6% (or ±0.41μs). Considering acquisition parameters resembling our experimental setup and assuming diffraction limited excitation volume of e.g. ~2μm^3, zero background emission and shot noise limit detection, a measurement of such kind can be in principle accomplished within just ~20ms of data averaging. In practice, however, longer acquisition periods are typically required due to higher noise levels and/or variations in instrumentation parameters.

Imaging depth.—The emission band of Oxyphor 2P (Fig. 1D) is red-shifted by ~100 nm relative to that of PtP-C343 (Finikova et al., 2008), which should allow for deeper imaging. To assess the depth limit we injected Oxyphor 2P into the blood and compared the intensity of the phosphorescence signal (quantified as the area under the decay curve) measured while focusing the laser on a point within a blood vessel at a given depth *vs* that measured when focusing on a neighboring point in the extra-vascular space (Fig. 2G). Since the blood-brain barrier completely prevents diffusion of the probe into the parenchyma, any signal originating seemingly from the extravascular space has to arise due to out-of-focus excitation. In the case of PtP-C343 out-of-focus phosphorescence was appreciable already at depths ~300μm (Lecoq et al., 2011), however, Oxyphor 2P allowed imaging down to 600μm with >90% of the signal coming exclusively from the focal volume (Fig. 2H), effectively increasing imaging depth by two times.

Minimally invasive delivery of Oxyphor 2P to the brain tissue

For extravascular (tissue) pO_2 measurements, previously probes were pressure injected directly into the imaged region of the cortex (Devor et al., 2011; Lecoq et al., 2011; Sakadzic et al., 2010). That could potentially cause cell damage, triggering reactive gliosis and related metabolic changes, influencing local pO_2 (Davalos et al., 2005). Although Oxyphor 2P also can be delivered by this traditional method, here we explored a different approach, which takes advantage of exceptional brightness of the new probe. A small volume of the concentrated solution of the probe was injected into the *cisterna magna* far away from the measurement site. The probe that reached the cortex by way of diffusion in the cerebrospinal fluid (CSF) was sufficient for pO_2 measurements (Supplemental Information, Fig. S3). Thus, we were able to image oxygen in the intravascular space below the cortical surface, while completely avoiding tissue damage in the imaged location. It is important to note that this administration approach is particularly valuable for use in chronic cranial windows, because the window does not need to be re-opened for injections, which could potentially lead to tissue infections in addition to the damage caused by introducing a micropipette.

It is worth noting that upon delivery into *cisterna magna* the probe remains in the brain tissue and generates strong signals even days after injection. The clearance rate was in fact

so low that it could not be inferred from the measurements of the phosphorescence intensity during one imaging session. Accurate quantification of the clearance kinetics will require harvesting of the brain tissue and measuring the probe concentration using tissue homogenate. These studies will be performed in the future.

Longitudinal measurements: imaging pO_2 dynamics after micro-stroke

Sudden disruption of blood supply to parts of the brain causes detrimental and often irreversible tissue damage, leading to loss of function. One clinically important and common cause of such disruption is micro-strokes. Micro-strokes, which occur at the level of small arterioles or capillaries, are localized, often microscopically sized infarctions. There is increasing evidence that micro-strokes are associated with cognitive impairment in their own right, as well as being a symptom of small vessel disease (van Veluw et al., 2017).

Due to the relatively high rate of oxygen consumption in the brain, discontinuation of oxygen transport upon stroke leads to a catastrophic drop in the energy supply, which occurs in a matter of seconds. Hence, to observe the acute changes caused by a stroke, fast imaging of oxygen dynamics is indispensable. On the other hand, while onset of stroke is rapid, changes in cellular function, tissue structure, and behavior that follow take place over a much longer timescale (days). Therefore, chronic measurements are necessary for better understanding of the pathophysiology of stroke and development of treatment strategies. Deep imaging is critical because both the most metabolically active and most stroke-prone regions are often located deep in the cortex (Weber et al., 2008) and even in the white matter.

Previously, longitudinal pO_2 measurements in the brain using 2PLM were extremely challenging, since low emissivity of PtP-C343 necessitated re-injection of the probe into the imaged region in order to maintain adequate signal levels. Multiple injections inevitably led to tissue damage, obscuring results. In order to demonstrate the potential of Oxyphor 2P for chronic imaging, we performed an experiment using the method of probe delivery through injection into the *cisterna magna*, as described above. Using this approach, we could measure extravascular pO_2 for days following a single probe injection (Fig. 3). Subsequent injections also could be performed, in the same animal away from the measurement site, and no adverse effects were observed.

The micro-stroke was created by irradiating a selected capillary with a focused laser beam. Shortly after the stroke induction, we observed a drop in pO_2 in the immediate stroke region and 200 μm around the lesion, accompanied by a leakage of the blood plasma marker (FITC-dextran) into the extravascular space. Interestingly, this hypoxic region recovered to a pre-stroke pO_2 within 4 days, and the repair of the vessel could be observed in the corresponding angiographic image.

In conclusion, the new probe Oxyphor 2P represents a major step forward for oxygen imaging technology and significantly extends the scope of pO_2 imaging applications. First, very high brightness of Oxyphor 2P results in a dramatic ~60 times increase in measurement speed that will be beneficial for functional studies during transient changes in oxygenation. Secondly, Oxyphor 2P affords a 2-fold increase in imaging depth in brain cortex. Thirdly, Oxyphor 2P makes it possible to deliver the probe through the CSF, avoiding direct injection

and therefore enabling chronic tissue pO_2 measurements in the brain. Finally, the simpler structure of Oxyphor 2P and consequently simpler synthesis will render 2PLM more accessible to a broad biomedical community. In combination with the ever-increasing availability of two-photon microscopy, Oxyphor 2P should promote progress in many biomedical research fields.

Limitations

One of the intrinsic limitations of phosphorescence lifetime imaging is its relatively low speed compared to much more common fluorescence-based methods. Low imaging rates are due to long triplet lifetimes of phosphorescent molecules: microseconds *vs* nanoseconds for fluorescent chromophores. On the other hand, it is because of these long lifetimes phosphorescence is so exquisitely responsive to oxygen in the physiological oxygen range, while fluorescence is essentially oxygen-insensitive. While bright probes, such as Oxyphor 2P, enable faster imaging, 2PLM with high temporal resolution (per measurement point) is still limited to grid-like patterns rather than conventional 'smooth' pixel-to-pixel images. In most cases information obtained from such sparse grids is sufficient, since very steep oxygen gradients, which potentially can be missed in sparse maps, are unlikely to exist under normal physiological conditions. But in diseased states and/or in tissues with newly forming vasculature gradients may be higher, and imaging with higher pixel density still may be desirable. To this end, combing Oxyphor 2P with multifocal 2PLM (Howard et al., 2013) may significantly increase the overall image acquisition rates and allow for higher pixel density without jeopardizing temporal resolution. The key advantage of Oxyphor 2P is that unlike its predecessors (e.g. PtP-C343) it does not emit any fluorescence. The latter can be detrimental for phosphorescence lifetime measurements when multifocal 2PLM is implemented in frequency domain (Howard et al., 2013).

When fully PEGylated dendritic oxygen probes, such as Oxyphor 2P, are free in solution, the immediate environment of the chromophore is defined by the encapsulating dendrimer, while PEG residues make the probe chemically inert and prevent its binding to proteins, membranes etc. The calibration constants of such probes are completely sustained in biological environments, and oxygen measurements are quantitative. But because of the PEGylated shell these probes are unable to diffuse across biological membranes. For the purpose of measuring oxygenation in different tissue compartments this property presents an advantage; however, if one wants to append the probe to a particular biological target and/or deliver it inside a cell, suitable chemistries and delivery methods need to be developed.

In principle, modifying a phosphorescent probe in order to attach it to a targeting ligand or facilitate endocytosis is relatively straightforward, and many constructs of such kind have been reported in the literature (Kurokawa et al., 2015; Papkovsky and Dmitriev, 2013; Yoshihara et al., 2017). But unfortunately, lack of fully inert encapsulating shell inevitably leads to non-specific interactions of probes with endgenous macromolecules. In the resulting complexes, phosphorescent chromophores are shielded from oxygen, which results in strong and unpredictable changes in the probes' quenching properties. Consequently, all existing intracellular oxygen sensors are essentially non-quantitative and may show apparent heterogeneities in oxygen (e.g. steep intracellular oxygen gradients), where they do not exist,

but phosphorescence changes are induced by heterogeneities of the probe's local environment. Extensive chemical modifications of Oxyphor 2P with the purpose to label specific bio-molecules or facilitate its cellular uptake will likely jeopardize its inertness as well, resulting in the loss of quantitative imaging ability. Nevertheless, appending a chemical linker to the end of just one PEG residue, while maintaining the rest of the structure intact, may enable binding to a target without affecting the probe's quenching behavior. Methods for such modifications may be developed.

STAR METHODS

CONTACT FOR REAGENT AND RESOURCE SHARING

Further information and requests should be directed to and will be fulfilled by the Lead Contact, Sergei A. Vinogradov (vinograd.upenn@gmail.com).

EXPERIMENTAL MODEL AND SUBJECT DETAILS

Animal husbandry and all experimental and surgical procedures were approved by the local veterinary authorities (Veterinary Office, Canton of Zürich) and performed in accordance with Swiss law (Federal Act of Animal Protection 2005 and Animal Protection Ordinance 2008). Adult, female C57BL/6J mice (Charles River), 8–12 weeks old (20–25g) at the time of first surgery, were used for all experiments. The mice were housed together in individually ventilated cages of 2–4 littermates at approximately 25°C under an inverted 12 hour light/dark cycle, with food (M/R Haltung Extrudat, Granovit AG) and water ad libitum. During all surgical and experimental procedures the body temperature was kept constant at 37°C using a feedback-controlled heating pad (Harvard Apparatus) and the eyes were prevented from drying out with vitamin A ointment (Bausch & Lomb).

METHOD DETAILS

The synthesis and characterization of Oxyphor 2P are described in the Supplemental Information. The probe and the synthetic intermediates were characterized by standard analytical methods (^{1}H, ^{13}C NMR and mass-spectrometry) using commercial instrumentation.

Surgery—The surgical procedures have been described previously (Machler et al., 2016; Stobart et al., 2018). Briefly, animals were anaesthetised with isoflurane (Abbvie, 4% for induction, 1–2% for maintenance) and fixed in a stereotaxic frame (David Kopf Instruments). The skull was exposed, cleaned, and a bonding agent (Prime & Bond NT, Dentsply) was applied. Layers of light-cured dental cement (Synergy D6 Flow, Coltene) were applied to form a skull cap, leaving space over the left somatosensory cortex for the subsequent craniotomy. A custom-made aluminum headpost was fixed to the back of the skull cap with more dental cement. Surgical wounds were treated with antibiotic ointment (Cicatrex; Janssen-Cilag AG) and closed with tissue glue (Histoacryl, B. Braun). The mice were given analgesics (Buprenorphine, 0.1mg/kg subcutaneously during the day and 1mg/kg in drinking water overnight) and allowed to recover in their home cage. 24–48 hours later, the animals were anesthetised with a mixture of fentanyl (0.05 mg/kg, Sintenyl, Sintetica), midazolam (5 mg/kg, Dormicum, Roche), and medetomidine (0.5 mg/kg, Domitor, Orion

Pharma). This anaesthetic combination reduces the brain swelling common with isoflurane. A craniotomy was performed over the primary somatosensory cortex using a dental drill (Bien Air), and a square, 3×3 mm sapphire glass coverslip (ValleyDesign) was gently placed on the exposed, intact dura mater, and fixed to the skullcap with connecting agent (Signum connector, Heraeus Kulzer GmbH) and more dental cement to form a chronic cranial window. The mice were given analgesics as previously and allowed to recover in their home cage for at least 1 week prior to imaging. For the experiments shown in Fig. 2A–F the animals were lightly sedated with a combination of midazolam (5 mg/kg, subcutaneously) and isoflurane (0.5% in 200mL/min air). For the experiments in Fig. 2G–I and Fig. 3 the animals were anesthesized with isoflurane (0.5–2%). The pO_2 probes (Fig. 2) or FITC dextran (5%, 59–77kDa, Sigma) were injected into the blood *via* the tail vein. To inject into the cisterna magna (Iliff et al., 2012) the needle from a 26G syringe (B. Braun), bent ~3.5mm from the end of the needle to a ~40° angle (Ueda et al., 1979), was attached to a 10μl syringe *via* a length of polyurethane tubing (inner diameter 0.3mm, Putnam Plastics). After anaesthesizing the mouse, the head was bent forward, shaved if necessary, the needle was inserted into the cleft between the occiput and the atlas vertebra through the intact skin, muscles, and ligaments (Furlan et al., 2003) and ~10uL of the probe (initial conc. ~1.2mM) was injected.

Optical spectroscopy—Fluorescence and phosphorescence measurements were performed using a FS920 spectrofluorometer (Edinburgh Instruments), equipped with R2658P red-sensitive PMT (Hamamatsu). Both the excitation and the emission optical paths in the fluorometer were calibrated using a lamp with NIST-traceable spectral radiant flux (RS-15–50, Gamma Scientific, SN HL1956). The corresponding correction curves were used in all emission measurements. For quantum yield measurements absorbances of the samples at the excitation wavelengths were kept below 0.03 OD. The excitation and emission slits in the fluorometer were 1 nm. The quantum yields were determined relative to the phosphorescence of the PtTAPIP (ϕ_{phos}=0.45, 22°C, deoxygenated dimethylacetamide) (Esipova et al., 2016) as described previously (Esipova et al., 2016, 2017b).

Time-resolved phosphorescence measurements were carried out using a custom-made fiber-optic phosphorometer constructed around a multichannel data acquisition board (USB NI-6361, National Instruments) operating at 2 MHz frequency. The excitation sources in the instrument are light-emitting diodes (LED's) (LedEngin, LZ1), and the detector is an avalanche photodiode module (C12703, Hamamatsu). The luminescence decays were analyzed using non-linear least-squares method. The IRF of the instrument is ~1 μs (FWHM). All the custom software (hardware control, data collection and processing) was written in C/C++ (Qt, Nokia). Routine data analysis was performed using Origin 7.0 (OriginLab).

Concentrations of the samples for two-photon absorption measurements were 2–10 μM, corresponding to the absorbances in the Q-band maxima of the porphyrins of <0.5 OD. The 2PA spectrum of Oxyphor 2P was recorded by the 2P excitation method and referenced against the spectrum of PtTAPIP, as described previously (Esipova et al., 2016, 2017b). The sample of Oxyphor 2P was deoxygenated by argon bubbling (Airgas, Grade 5). A

Chameleon Ultra II laser (Coherent; pulse FWHM 110 fs, 80 MHz pulse repetition rate) was used as the excitation source.

To establish independence of the phosphorescence decay time on the excitation pathway (2P *vs* 1P), the probe solution in a quartz optical cell (1cm path length) was placed in a temperature controlled chamber (Quantum Northwest) and excited by short (~1μs-long) pulse trains from the laser at the wavelength matching the probe's 2PA maximum. The phosphorescence was collected in right-angle fashion, digitized and analyzed by single-exponential fitting. After that the phosphorescence decay probe was recorded under 1P excitation using the fiber-optic phosphorometer. These measurements were repeated at different temperatures, different probe concentrations and different oxygen concentrations (e.g. air, completely deoxygenated solutions). As expected, the resulting decay times were the same for 1P and 2P excitation pathways.

Probe synthesis

General information.: All solvents and reagents were purchased from commercial sources and used as received. mPEGAmine (MW 1000) was obtained from Laysan Bio, Inc. Size-exclusion chromatography (SEC) was performed using Bio-Beads S-X1 (40–80 μm bead size, Biorad). Column chromatography was performed using Selecto™ silica gel (Fisher Scientific). Analytical thin-layer chromatography (TLC) was carried out using silica gel matrix with a fluorescent indicator (layer thickness 200 m, particle size 25 m) on aluminum support (Sigma-Aldrich). ^{1}H and ^{13}C NMR spectra were recorded a spectrometer, operating at 400.1 MHz (^{1}H) or 100.6 MHz (^{13}C). Mass-spectra were recorded on a MALDI-TOF instrument, using α-cyano-4-hydroxycinnamicacid (CCA) as a matrix (positive-ion mode). Samples were prepared by mixing a solution of the analyte in THF or MeOH (10 μL, ~1 mM) with a solution of the matrix (100 μL, 10 mg/ml, 0.053 M) in THF. The sample, approximately 1 μL, was deposited on the probe tip, dried and analyzed. HRMS spectra were recorded on an ESI (electro-spray ionization) instrument using direct injection. Samples typically consisted of ~10 μM solution of the analyte compound in MeOH or THF/AcOH mixture (10:1).

Synthesis of glutamate/arylglycine dendrons.: The synthesis of dendron **4** (Scheme 1), which was used for modification of the core porphyrin (Scheme 2), consisted of a sequence of amide coupling/deprotection reactions. N-(*tert*-butoxycarbonyl)-3,5-dicarboxyphenyl glycineamide was synthesized as described previously (Vinogradov, 2005), and diallylglutamate *para*-tolune sulfonate was prepared by acid-catalyzed esterification of commercially available L-glutamic acid.

1. To a solution of N-(*tert*-butoxycarbonyl)-3,5-dicarboxyphenyl glycineamide (1.0 g, 3 mmol) in DMF (30 ml), cooled to 0°C, a solution of CDMT (1.31 g, 7.5 mmol) in DMF (5 ml) was added, followed by immediate addition of NMM (1 ml, 9 mmol). The reaction mixture was stirred at 0°C for 4 h, then a solution of diallylglutamate *para*-tolune sulfonate (2.37 g, 8.25 mmol) in DMF (30 ml) was added, and the reaction mixture was stirred at room temperature for 48 h. The solvent was removed in vacuum, the resulting oil was dissolved in CH_2Cl_2 (400 ml), washed with HCl aq. (1N, 200 ml), then with $NaHCO_3$ aq.

(10%, 2×200 ml) and dried over Na_2SO_4. The product was purified by column chromatography (silica gel, CH_2Cl_2/MeOH, 25:1) to give the title compound as yellowish solid. Yield 1.83 g (82%). ^{1}H NMR ($CDCl_3$, 60°C), δ (ppm): 1.47 (9H, s), 2.12–2.42 (4H, m), 2.49–2.65 (4H, m), 3.83–4.07 (2H, m), 4.47–4.73 (8H, m), 4.73–4.83 (2H, m), 5.09–5.44 (8H, m), 5.74–5.83 (1H, m), 5.83–6.00 (4H, m), 7.49–7.65 (2H, m), 7.67–7.76 (1H, m), 7.77–7.91 (2H, m), 8.79–9.09 (1H, m, broad). HRMS (ESI-TOF) m/z: $[M+H]^+$Calcd for $C_{37}H_{49}N_4O_{13}$ 757.3290; Found 757.3297.

2. To a solution of **1** (1.8 g, 2.38 mmol) in CH_2Cl_2 (20 ml), cooled to 0°C, trifluoroacetic acid (20 ml) was added slowly (over 5 min), and the reaction mixture was stirred overnight at room temperature. The solution was concentrated in vacuum. The resulting oil was dissolved in CH_2Cl_2 (150 ml), washed with water (75 ml), then with $NaHCO_3$ aq. (10%, 2×75 ml), finally with brine (75 ml) and dried over Na_2SO_4. The solvent was evaporated to give the title compound as a light-yellow solid. Yield: 1.33 g, 85%). ^{1}H NMR ($CDCl_3$, 60°C), δ (ppm): 2.09–2.39 (4H, m, -C*H*$_2$), 2.47–2.57 (4H, m, -C*H*$_2$), 3.47 (2H, s, broad, -N*H*$_2$), 3.77 (1H, s, broad, -C*H*H), 4.09–4.17 (1H, m, -CH*H*), 4.53–4.71 (8H, m, -C*H*$_2$), 4.76–4.85 (2H, m, -C*H*), 5.15–5.38 (8H, m, -C*HH*), 5.81–5.97 (4H, m, -C*H*), 7.29–7.48 (2H, m, Ar), 7.80–7.87 (1H, m, Ar), 8.01–8.10 (2H, m, broad, -N*H*), 9.08–9.67 (1H, m, broad, -N*H*). ^{13}C NMR ($CDCl_3$, 60°C), δ (ppm): 27.2, 30.6, 45.3, 52.6, 65.4, 66.2, 118.2, 118.9, 120.9, 131.7, 132.2, 134.9, 137.5, 138.7, 166.3, 171.3, 171.8, 172.4. HRMS (ESI-TOF) m/z: $[M+H]^+$Calcd for $C_{32}H_{41}N_4O_{11}$ 657.2766; Found 657.2770.

3. To a solution of N-(*tert*-butoxycarbonyl)-L-glutamic acid (0.206 g, 0.834 mmol) in DMF (10 ml), HBTU (0.7 g, 1.845 mmol) was added, and the reaction mixture was stirred for 10 min at room temperature. A solution of **2** (1.15 g, 1.75 mmol) and DIPEA (0.6 ml, 3.4 mmol) in DMF (20 ml) was added to the mixture, and it was allowed to react under stirring at room temperature for 48 h. The resulting mixture was poured into water (100 ml), and the formed yellow oil was collected by centrifugation, washed with water (2×100 ml) and dried in vacuum. The product was purified by column chromatography (silica gel, CH_2Cl_2/MeOH, 20:1) to give the title compound as yellowish solid. Yield: 0.95 g (75%). ^{1}H NMR ($CDCl_3$, 60°C), δ (ppm): 1.34 (9H, s, -C(O)(C*H*$_3$)$_3$), 2.07–2.45 (10H, m, -C*H*$_2$), 2.45–2.71 (10H, m, -C*H*$_2$), 3.92–4.38 (4H, m, -C*H*$_2$), 4.48–4.76 (17H, m, -C*H*$_2$, -C*H*), 4.76–4.86 (4H, m, -C*H*H), 5.12–5.41 (16H, m, -C*H*$_2$), 5.80–6.01 (9H, m, -C*H*, -N*H*), 7.55–8.01 (12H, m, Ar, -N*H*), 9.08–9.28 (2H, m, broad, -N*H*).

4. To a solution of the **3** (0.9 g, 0.59 mmol) in CH_2Cl_2(10 ml), cooled to 0°C, trifluoroacetic acid (10 ml) was added slowly (over 5 min), and the reaction mixture was stirred overnight at room temperature. The solution was concentrated in vacuum. The resulting oil was dissolved in CH_2Cl_2 (150 ml), washed with water (75 ml), then with aq. $NaHCO_3$ (10%, 2×75 ml), finally with brine (75 ml) and dried over Na_2SO_4. The solvent was evaporated in vacuum, and the product was purified by column chromatography (silica gel, CH_2Cl_2/MeOH, gradient 20:1–10:1) to give the title compound as a yellow solid. Yield: 0.675 g, 80%. ^{1}H NMR (DMSO-d_6, 80°C), δ (ppm): 1.63–1.76 (1H, m, -C*H*H), 1.88–1.98 (1H, m, -CH*H*), 2.02–2.23 (8H, m, -C*H*$_2$), 2.27–2.35 (2H, m, -C*H*$_2$), 2.45–2.52 (8H, m, -C*H*$_2$), 2.97–3.11 (1H, m, broad, -N*H*H), 3.24–3.33 (1H, s, broad, -NH*H*), 3.83–4.00 (4H, m, -C*H*$_2$), 4.00–4.17 (1H, m, -C*H*), 4.49–4.64 (20H, m, -C*H*$_2$, -C*H*), 5.14–5.36 (16H, m, -C*HH*), 5.81–

5.97 (8H, m, -C*H*), 7.86–8.09 (4H, m, Ar, -N*H*), 8.10–8.21 (4H, m, broad, -N*H*), 8.60–8.76 (4H, m, Ar), 9.92–10.13 (2H, m, broad, -N*H*). ^{13}C NMR (DMSO-d_6, 80°C), δ (ppm): 25.6, 29.8, 30.6, 31.6, 42.4, 42.5, 51.9, 54.1, 64.0, 64.5, 117.2, 117.3, 120.85, 120.90, 121.2, 132.0, 132.3, 134.6, 138.4, 138.5, 166.04, 166.06, 167.7, 167.9, 170.7, 171.3, 172.3, 175.0. HRMS (ESI-TOF) m/z: $[M+H]^+$Calcd for $C_{69}H_{86}N_9O_{24}$ 1424.5779; Found 1424.5792.

Assembly of Oxyphor 2P.: The synthesis of the core porphyrin (PtTAPIP) followed the earlier developed method (Esipova et al., 2017a).

Porphyrin-dendrimer **5**. To a solution of PtTAPIP (0.090 g, 0.043 mmol) in DMF (20 ml), HBTU (0.165 g, 0.435 mmol) was added, and the reaction mixture was stirred for 10 min at room temperature. A solution of dendron **4** (0.640 g, 0.445mmol) and DIPEA (0.3 ml, 1.73mmol) in DMF (40 ml) was added to the mixture, and it was stirred at room temperature for 72 h. The progress of the reaction was monitored every 24 h by MALDI-TOF analysis, and the small portions of HBTU (0.05 g, 0.13 mmol) were added to the mixture until the reaction was. The reaction mixture was poured into aqueous solution of HCl (5%, 100 ml), and the green precipitate formed was collected by centrifugation, washed with water (2×100 ml) and dried in vacuum. After purification by SEC using THF as a mobile phase, the title porphyrindendrimer was isolated as a bright-green solid. Yield: 0.54 g (94%). NMR ^{1}H (DMSO-d_6, 80°C), δ, ppm: 1.91–2.20 (96H, m), 2.24–2.34 (32H, m), 2.38–2.47 (64H, m), 3.82–3.97 (32H, m), 4.11–4.19 (16H, m), 4.27–4.34 (8H, m), 4.46–4.61 (160H, m), 5.10–5.32 (128H, m), 5.75–5.97 (64H, m), 6.84–6.97 (8H, m), 7.40–7.51 (4H, m), 7.84–8.18 (72H, m), 8.54–8.68 (32H, m), 9.85–10.02 (16H, m), 10.66–10.76 (8H, s, broad), 12.15–12.25 (4H, s, broad, *meso*-H). MALDI-TOF (*m/z*): calcd for $C_{660}H_{760}N_{80}O_{216}Pt$13456.06, found 13494.98 $[M+K]^+$, fragment ions: 13349.13, 12690.53, 12020.99, 11311.20, 10641.24.

Porphyrin-dendrimer **6**. To a solution of **5** (0.5 g, 0.037 mmol) in DMF (30 ml), Pd(0)$(PPh_3)_4$ (0.151 g, 0.13 mmol) was added, followed by the addition of morpholine (1.16 ml, 13.4 mmol), and the reaction mixture was stirred at room temperature for 5–7 days. The progress of the reaction was monitored by MALDI-TOF analysis every 24 h. Small portions of Pd(0)$(PPh_3)_4$ (0.03 g, 0.0026mmol) were added to the mixture if deprotection was incomplete, and the reaction continued. The reaction mixture was poured into aqueous solution of HCl (5%, 200 ml), and the green precipitate formed was collected by centrifugation, washed with water (2×100 ml) and dried in vacuum. To the resulting green solid, TFA (40 ml) was added, and the white precipitate formed (contamination) was removed by centrifugation. TFA was removed in vacuum, and the title compound was isolated as a green solid, which was used in the following step without further purification. Yield: 0.375 g (93%). MALDI-TOF (*m/z*): calcd for $C_{468}H_{504}N_{80}O_{216}Pt$ 10900.07, found fragment ions: 10734.47, 10140.67, 9577.74, 9039.84.

Oxyphor 2P.: To a solution of **6** (0.375 g, 0.0344mmol) in DMF (50 ml), HBTU (1.04 g, 2.75mmol) was added, and the reaction mixture was stirred for 10 min at room temperature. A solution of methoxypolyethyleneglycol amine (mPEG-amine, Av MW 1000, 2.75 g, 2.75 mmol) and DIPEA (1.9 ml, 11 mmol) in DMF (30 ml) was added, and the reaction mixture was stirred at room temperature for 5–7 days. The progress of the reaction was monitored by

MALDI-TOF analysis every 24 h, and the small portions of HBTU (0.2 g, 0.53 mmol) were added to the mixture until the reaction was complete. The crude was subjected to SEC using THF as a mobile phase, yielding **Oxyphor 2P** as a bright-green solid after evaporation of the solvent. Yield: 2.0 g, 80%. MALDI-TOF (m/z): calc. for $C_{3348}H_{6328}N_{144}O_{1560}Pt$: 73715.97, found: range from ~43000 to ~70000 with maximum at 57074 (the theoretical molecular formula and molecular weight were calculated assuming 1) the formula $C_{45}H_{93}NO_{22}$ (MW 999) for mPEG-amine and 2) that every one of 64 carboxyl groups on **6** was PEGylated.

Probe calibrations—A cylindrical vial with solution of a probe (~2–5μM) was sealed with silicon rubber stopper, through which an oxygen electrode (CK, 4 pA current at zero oxygen) and two stainless steel needles, serving as gas inlet and outlet, were inserted. The vial held approximately 10 ml of liquid and it was slightly underfilled, so that a flow of inert gas (nitrogen or argon) could be passed over the solution surface. The vial was placed into a temperature-controlled chamber (±0.1°C precision), equipped with a magnetic stirrer, and the excitation and collection fibers were positioned at 90° to one-another up against the vial wall inside the chamber. The electrode current was amplified and digitized, and the readings were recorded into a file. Phosphorescence decays were measured using the fiber-optic phosphorometer (see above) and logged into another file. As inert gas was passed over the surface of the stirred solution, gradually replacing O_2 and other dissolved gasses, synchronous recordings of the phosphorescence decays and electrode current provided the raw data for the subsequent analysis. The phosphorescence was excited by 10μs-long light pulses and collected/digitized during 1 ms. The first 5μs of the data (after the falling edge of the excitation pulse) were rejected to avoid interference of the IRF with the decay analysis. The decays were analyzed by single-exponential fitting, while the electrode current at each point was converted into the corresponding partial pressure of oxygen (pO_2) assuming the atmospheric pressure of 760 mmHg, 21% O_2 content in the atmosphere and taking into account partial pressure of water vapor at the solution temperature. After the phosphorescence lifetime stopped changing and the electrode current was essentially zero, the calibration was stopped. Typically, 500–700 data points (phosphorescence decay *vs* electrode current) were recorded in each titration run.

The resulting plots of pO_2 *vs* phosphorescence decay time of Oxyphor 2P (at different temperatures, pH and other examined conditions) were fit to an empirical equation:

$$pO_2(\tau, T) = \frac{1}{k_q(T)}\left(\frac{1}{a \times \tau^p} - \frac{1}{\tau_0}\right), \quad \text{(Eq. 1)}$$

which resembles the classic Stern-Volmer formula. In Eq. 1, τ_0 (the decay time at pO_2=0), empirical parameter p and coefficient a remain constant throughout the physiological temperature range: τ_0=3.8×10-^{5} s, p=1.265777 and a=14.8, while the quenching constant k_q changes linearly with temperature (Fig. 1) as:

$$k_q(T) = k_q^0 + \beta T, \quad \text{(Eq. 2)}$$

where k_q^0=91.01153 and β=19.43017.

For most titration experiments (e.g. Fig. 1E–G) the probe was dissolved in a standard phosphate buffer saline (PBS) solution at ~1μM concentration. The pH of the solution was adjusted by small additions of either HCl or NaOH. Alternatively, the probe was dissolved directly in the rat blood plasma (Fig. 1e). For determining the influence of metal ions (Supplemental Information, Fig. S2), the probe was dissolved in distilled water, and stock solutions of salts ($CaCl_2$, $ZnCl_2$ and $MgCl_2$) were added to reach the final concentrations of 20mM.

Two-photon microscopy—Two-photon imaging was performed using a custom-built microscope, which has been described previously (Mayrhofer et al., 2015). Briefly, fluorescence and phosphorescence were excited simultaneously using a Ti:sapphire laser (80 MHz, <120 fs pulse width, Insight DS+, Spectra-Physics) tuned to 950 nm for Oxyphor 2P or 920 nm for PtP-C343, directed by galvanometric scanners (6215H, Cambridge Technology) and focused with a 16× (Apochromat 0.8NA DIC, Nikon) or 20× (W-Plan-Apochromat 1.0NA DIC, Zeiss) water-immersion objective. The microscope motion, including motorized rotation to align with the cortical surface, was controlled with custom-designed LabView software (National Instruments) and the imaging was controlled using a version of ScanImage (Pologruto et al., 2003) that had been modified in house to enable gating the laser output during imaging (which is necessary for phosphorescence lifetime imaging), as well as customized scan paths. Each phosphorescence excitation/collection cycle consisted of a 10μs-long train of femtosecond pulses (800 pulses), followed by a 260 μs-long period for collection of the phosphorescence photons. A dead time of 10 μs was appended to the end of each cycle due to software limitations, so that each cycle was effectively 280 μs-long. Movement of the galvo-scanner between two consecutive locations typically required <0.3 ms and was included in the imaging time. Thus, a measurement in 12 locations (such as in Fig. 2B,C) with averaging of 150 cycles per location required ~0.5s, during which the effective data collection time per location was 42 ms. The emitted light was reflected by a dichroic mirror (short-pass, 825nm central wavelength, Chroma) into a 4 channel detection system, where the phosphorescence channel was isolated using 760±25nm bandpass filter (Oxyphor 2P, Chroma) or 690±25nm filter (PtP-C343, Chroma) and detected by a highly sensitive photomultiplier tube (PMT; H10770PA-50 SEL, Hamamatsu). The PMT signal was digitized by an analog-to-digital converter operating at 1 MHz frequency. Typically, the time-averaged laser power under the objective during application of the pulse train was ~24 mW. To induce the localized stroke, the laser was focused at high power (>50 mW) on a small line along the blood vessel lumen until the passage of RBCs was no longer observed. Phosphorescence lifetimes were calculated by fitting the decays with single-exponentials using nonlinear least squares, and the standard error in the lifetimes was estimated with a bootstrap resampling approach. The lifetimes and standard errors were converted to pO_2 measurements using a Stern-Volmer-like calibration plot, obtained as described above.

Theoretical estimation of 2PLM temporal resolution (an example)—Consider pO_2 measurements near 20 mmHg with ±1 mmHg accuracy. The Stern-Volmer oxygen

quenching parameters of Oxyphor 2P parameters are as follows: τ_0=38 μs, k_q ~593 mmHg $^{-1}s^{-1}$ and the quantum yield in the absence of oxygen of ϕ_0=0.23. Using the Stern-Volmer equation ($1/\tau=1/\tau_0+k_q \times pO_2$), we obtain the lifetime τ and the quantum yield ϕ at 20 mmHg as 26.6 μs and 0.16, respectively. In order to achieve the desired level of accuracy in the pO_2 measurement we need to be able to determine phosphorescence lifetimes with accuracy of $\delta\tau$~±0.41 μs or ±1.6%:

$$\delta\tau = \tau\,(19\text{mmHg}) - \tau\,(20\text{mmHg}) = 0.41\mu\text{s}\text{ , where}$$

$$\tau\left(pO_2\right) = \frac{\tau_0}{1 + k_q\,\tau_0\,pO_2}\ .$$

For the ideal case of single-exponential decay, photon-counting detection, zero background and shot noise limit, and considering the decay acquisition window of 270 μs, as in our experiments, the desired accuracy in the lifetime determination requires collection of M≈4160 photons (Kollner and Wolfrum, 1992):

$$M(\tau,\ \delta\tau, r, k) := \frac{\tau^2}{\delta\ \tau^2} \cdot \frac{k^2}{r^2} \cdot (1 - \exp(-r)) \cdot \left[\left[\frac{\exp\left(\frac{r}{k}\right)(1 - \exp(-r))}{\left(\exp\left(\frac{r}{k}\right) - 1\right)^2}\right] - \frac{k^2}{\exp(r) - 1}\right]^{-1}$$

$M(\tau, \delta\tau, r, k) = 4.162 \cdot_{10} 3$, where T=270 μs - data acquisition cycle, $r=T/\tau$≈10.5 - number of decay times per acquisition cycle and k=270 - number of bins for photon collection per acquisition cycle.

If the probe concentration is 10μM, excitation volume of ~2μm^3 contains ~12000 probe molecules. Considering e.g. 50% triplet saturation (to maintain the excitation volume sufficiently close to diffraction limited (Sinks et al., 2010b)), collection efficiency of 10%, detector quantum efficiency of 0.6 and the probe quantum yield of 0.16, 58 photons will be measured by the detector after one excitation cycle. Thus, one would have to average ~72 acquisition cycles to reach the desired number of photons, which will take ~19ms (270 μs per cycle).

QUANTIFICATION AND STATISTICAL ANALYSIS

Statistical analysis was conducted using R (version 3.4.1, R Core Team, 2017). For simple comparisons, standard t-tests (after checking for normality) or non-parametric tests were used, as described in the main text. Linear mixed effects models (Bates et al., 2015) were used to analyze the differences between the error measured with the two probes (Fig. 2E), the baseline pO_2 (Fig. 2F), and the tissue pO_2 values following micro-stroke (Fig. 3C). Each unique combination of probe and amount of data analyzed (i.e. each bar in Fig. 2E and Fig 2F) or each time point (Fig. 3C) was specified as a fixed effect, and intercepts for each mouse were specified as random effects. Based on visual inspection of the residual plots, the data were log-transformed to correct for deviations from homoscedasticity and/or normality when necessary. P-values for the overall significance of an effect were determined by

likelihood ratio tests of the full model with the effect in question against a model without the effect in question. P-values for differences between groups were obtained post-hoc using the Tukey correction for multiple comparisons (Hothorn et al., 2008).

Supplementary Material

Refer to Web version on PubMed Central for supplementary material.

ACKNOWLEDGMENTS

This work was supported by the grants EB018464 and NS092986 from the National Institutes of Health, USA (S.A.V.), the Forschungskredit of the University of Zurich (M.J.P.B.) and a grant from the Russian Science Foundation (contract #14–43–00052), operated by the Center of Photochemistry, Russian Academy of Sciences (A.E.M.). B.W. is supported by the University of Zurich and the Swiss National Science Foundation. The authors are grateful to Dr. Matthias Wyss for assistance with vascular pO_2 measurements.

REFERENCES

Bates D, Machler M, Bolker BM, and Walker SC (2015). Fitting linear mixed-effects models using lme4. J. Stat. Softw 67, 1–48.

Brinas RP, Troxler T, Hochstrasser RM, and Vinogradov SA (2005). Phosphorescent oxygen sensor with dendritic protection and two-photon absorbing antenna. J. Am. Chem. Soc 127, 11851–11862. [PubMed: 16104764]

Ceroni P, Lebedev AY, Marchi E, Yuan M, Esipova TV, Bergamini G, Wilson DF, Busch TM, and Vinogradov SA (2011). Evaluation of phototoxicity of dendritic porphyrin-based phosphorescent oxygen probes: an in vitro study. Photochem. & Photobiol. Sci 10, 1056–1065. [PubMed: 21409208]

Choi NW, Verbridge SS, Williams RM, Chen J, Kim JY, Schmehl R, Farnum CE, Zipfel WR, Fischbach C, and Stroock AD (2012). Phosphorescent nanoparticles for quantitative measurements of oxygen profiles in vitro and in vivo. Biomaterials 33, 2710–2722. [PubMed: 22240511]

Davalos D, Grutzendler J, Yang G, Kim JV, Zuo Y, Jung S, Littman DR, Dustin ML, and Gan WB (2005). ATP mediates rapid microglial response to local brain injury in vivo. Nat. Neurosci 8, 752–758. [PubMed: 15895084]

Devor A, Sakadzic S, Saisan PA, Yaseen MA, Roussakis E, Srinivasan VJ, Vinogradov SA, Rosen BR, Buxton RB, Dale AM, and Boas DA (2011). “Overshoot” of O2 is required to maintain baseline tissue oxygenation at locations distal to blood vessels. J. Neurosci 31, 13676–13681. [PubMed: 21940458]

Erecinska M, and Silver IA (2001). Tissue oxygen tension and brain sensitivity to hypoxia. Respiration physiology 128, 263–276. [PubMed: 11718758]

Esipova TV, Karagodov A, Miller J, Wilson DF, Busch TM, and Vinogradov SA (2011). Two new “protected” oxyphors for biological oximetry: properties and application in tumor imaging. Anal. Chem 83, 8756–8765. [PubMed: 21961699]

Esipova TV, Rivera-Jacquez HJ, Weber B, Masunov AE, and Vinogradov SA (2016). Two-photon absorbing phosphorescent metalloporphyrins: effects of **π**-extension and peripheral substitution. J. Am. Chem. Soc 138, 15648–15662. [PubMed: 27934026]

Esipova TV, Rivera-Jacquez HJ, Weber B, Masunov AE, and Vinogradov SA (2017a). Stabilizing *g*-States in Centrosymmetric Tetrapyrroles: Two-Photon-Absorbing Porphyrins with Bright Phosphorescence. J. Phys. Chem. A, 10.1021/acs.jpca.1027b04333.

Esipova TV, Rivera-Jacquez HJ, Weber B, Masunov AE, and Vinogradov SA (2017b). Stabilizing *g*-states in centrosymmetric tetrapyrroles: two-photon-absorbing porphyrins with bright phosphorescence. J. Phys. Chem. A 121, 6243–6255. [PubMed: 28766943]

Finikova OS, Lebedev AY, Aprelev A, Troxler T, Gao F, Garnacho C, Muro S, Hochstrasser RM, and Vinogradov SA (2008). Oxygen microscopy by two-photon-excited phosphorescence. Chemphyschem 9, 1673–1679. [PubMed: 18663708]

Finikova OS, Troxler T, Senes A, DeGrado WF, Hochstrasser RM, and Vinogradov SA (2007). Energy and electron transfer in enhanced two-photon-absorbing systems with triplet cores. J. Phys. Chem. A 111, 6977–6990. [PubMed: 17608457]

Furlan R, Pluchino S, Marconi PC, and Martino G (2003). Cytokine gene delivery into the central nervous system using intrathecally injected nonreplicative viral vectors. Methods in molecular biology 215, 279–289. [PubMed: 12512306]

Ham PB, 3rd, and Raju R (2017). Mitochondrial function in hypoxic ischemic injury and influence of aging. Progress in neurobiology 157, 92–116. [PubMed: 27321753]

Hothorn T, Bretz F, and Westfall P (2008). Simultaneous inference in general parametric models. Biometrical journal. Biometrische Zeitschrift 50, 346–363. [PubMed: 18481363]

Howard SS, Straub A, Horton NG, Kobat D, and Xu C (2013). Frequency-multiplexed *in vivo* multiphoton phosphorescence lifetime microscopy. Nature Photonics 7, 33–37. [PubMed: 23472061]

Iliff JJ, Wang M, Liao Y, Plogg BA, Peng W, Gundersen GA, Benveniste H, Vates GE, Deane R, Goldman SA, Nagelhus EA, and Nedergaard M (2012). A paravascular pathway facilitates CSF flow through the brain parenchyma and the clearance of interstitial solutes, including amyloid beta. Science translational medicine 4, 147ra111.

Kazmi SMS, Salvaggio AJ, Estrada AD, Hemati MA, Shaydyuk NK, Roussakis E, Jones TA, Vinogradov SA, and Dunn AK (2013). Three-dimensional mapping of oxygen tension in cortical arterioles before and after occlusion. Biomed. Opt. Express 4, 1061–1073. [PubMed: 23847732]

Khan AA, Vigil GD, Zhang YD, Fullerton-Shirey SK, and Howard SS (2017). Silica-coated ruthenium-complex nanoprobes for two-photon oxygen microscopy in biological media. Opt. Mater. Express 7, 1066–1076.

Kollner M, and Wolfrum J (1992). How many photons are necessary for fluorescence lifetime measurements. Chem. Phys. Lett 200, 199–204.

Kurihara T, Westenskow PD, Gantner ML, Usui Y, Schultz A, Bravo S, Aguilar E, Wittgrove C, Friedlander MSH, Paris LP, Chew E, Siuzdak G, and Friedlander M (2016). Hypoxia-induced metabolic stress in retinal pigment epithelial cells is sufficient to induce photoreceptor degeneration. eLife 5, e14319. [PubMed: 26978795]

Kurokawa H, Ito H, Inoue M, Tabata K, Sato Y, Yamagata K, Kizaka-Kondoh S, Kadonosono T, Yano S, Inoue M, and Kamachi T (2015). High resolution imaging of intracellular oxygen concentration by phosphorescence lifetime. Scientific Reports 5.

Lebedev AY, Cheprakov AV, Sakadzic S, Boas DA, Wilson DF, and Vinogradov SA (2009). Dendritic phosphorescent probes for oxygen imaging in biological systems. ACS Appl. Materials & Interfaces 1, 1292–1304.

Lebedev AY, Filatov MA, Cheprakov AV, and Vinogradov SA (2008). Effects of structural deformations on optical properties of tetrabenzoporphyrins: free-bases and Pd complexes. J. Phys. Chem. A 112, 7723–7733. [PubMed: 18665576]

Lecoq J, Parpaleix A, Roussakis E, Ducros M, Houssen YG, Vinogradov SA, and Charpak S (2011). Simultaneous two-photon imaging of oxygen and blood flow in deep cerebral vessels. Nat. Medicine 17, 893–U262.

Lemon CM, Karnas E, Han X, Bruns OT, Kempa TJ, Fukumura D, Bawendi MG, Jain RK, Duda DG, and Nocera DG (2015). Micelle-encapsulated quantum dot-porphyrin assemblies as *in vivo* two-photon oxygen sensors. J. Am. Chem. Soc 137, 9832–9842. [PubMed: 26149349]

Lyons DG, Parpaleix A, Roche M, and Charpak S (2016). Mapping oxygen concentration in the awake mouse brain. eLife 5.

Machler P, Wyss MT, Elsayed M, Stobart J, Gutierrez R, von Faber-Castell A, Kaelin V, Zuend M, San Martin A, Romero-Gomez I, Baeza-Lehnert F, Lengacher S, Schneider BL, Aebischer P, Magistretti PJ, Barros LF, and Weber B (2016). *In vivo* evidence for a lactate gradient from astrocytes to neurons. Cell metabolism 23, 94–102. [PubMed: 26698914]

Mayrhofer JM, Haiss F, Haenni D, Weber S, Zuend M, Barrett MJ, Ferrari KD, Maechler P, Saab AS, Stobart JL, Wyss MT, Johannssen H, Osswald H, Palmer LM, Revol V, Schuh CD, Urban C, Hall A, Larkum ME, Rutz-Innerhofer E, Zeilhofer HU, Ziegler U, and Weber B (2015). Design and

performance of an ultra-flexible two-photon microscope for *in vivo* research. Biomed. Opt. Express 6, 4228–4237. [PubMed: 26600989]

Papkovsky DB, and Dmitriev RI (2013). Biological detection by optical oxygen sensing. Chemical Society Reviews 42, 8700–8732. [PubMed: 23775387]

Parpaleix A, Houssen YG, and Charpak S (2013). Imaging local neuronal activity by monitoring pO_2 transients in capillaries. Nat. Medicine 19, 241–246.

Pologruto TA, Sabatini BL, and Svoboda K (2003). *ScanImage*: flexible software for operating laser scanning microscopes. Biomedical engineering online 2, 13. [PubMed: 12801419]

Quaranta M, Borisov SM, and Klimant I (2012). Indicators for optical oxygen sensors. Bioanal. Rev 4, 115–157. [PubMed: 23227132]

Ratcliffe PJ (2013). Oxygen sensing and hypoxia signalling pathways in animals: the implications of physiology for cancer. The Journal of physiology 591, 2027–2042. [PubMed: 23401619]

Roussakis E, Spencer JA, Lin C, and Vinogradov SA (2014). Two-photon antenna-core oxygen probe with enhanced performance. Anal. Chem 86, 5937–5945. [PubMed: 24848643]

Rumsey WL, Vanderkooi JM, and Wilson DF (1988). Imaging of phosphorescence: a novel method for measuring the distribution of oxygen in perfused tissue. Science 241, 1649–1651. [PubMed: 3420417]

Sakadzic S, Mandeville ET, Gagnon L, Musacchia JJ, Yaseen MA, Yucel MA, Lefebvre J, Lesage F, Dale AM, Eikermann-Haerter K, Ayata C, Srinivasan VJ, Lo EH, Devor A, and Boas DA (2014). Large arteriolar component of oxygen delivery implies a safe margin of oxygen supply to cerebral tissue. Nat. Commun 5.

Sakadzic S, Roussakis E, Yaseen MA, Mandeville ET, Srinivasan VJ, Arai K, Ruvinskaya S, Devor A, Lo EH, Vinogradov SA, and Boas DA (2010). Two-photon high-resolution measurement of partial pressure of oxygen in cerebral vasculature and tissue. Nat. Methods 7, 755–U125. [PubMed: 20693997]

Sinks LE, Robbins GP, Roussakis E, Troxler T, Hammer DA, and Vinogradov SA (2010a). Two-photon microscopy of oxygen: polymersomes as probe carrier vehicles. J. Phys. Chem. B 114, 14373–14382. [PubMed: 20462225]

Sinks LE, Robbins GP, Roussakis E, Troxler T, Hammer DA, and Vinogradov SA (2010b). Two-photon microscopy of oxygen: polymersomes as probe carrier vehicles. Journal of Physical Chemistry B 114, 14373–14382.

Spencer JA, Ferraro F, Roussakis E, Klein A, Wu JW, Runnels JM, Zaher W, Mortensen LJ, Alt C, Turcotte R, Yusuf R, Cote D, Vinogradov SA, Scadden DT, and Lin CP (2014). Direct measurement of local oxygen concentration in the bone marrow of live animals. Nature 508, 269. [PubMed: 24590072]

Stobart JL, Ferrari KD, Barrett MJP, Stobart MJ, Looser ZJ, Saab AS, and Weber B (2018). Long-term *in vivo* calcium imaging of astrocytes reveals distinct cellular compartment responses to sensory stimulation. Cereb. Cortex 28, 184–198. [PubMed: 28968832]

Tsai AG, Johnson PC, and Intaglietta M (2003). Oxygen gradients in the microcirculation. Physiol. Rev 83, 933–963. [PubMed: 12843412]

Ueda H, Amano H, Shiomi H, and Takagi H (1979). Comparison of the analgesic effects of various opioid peptides by a newly devised intracisternal injection technique in conscious mice. European journal of pharmacology 56, 265–268. [PubMed: 582583]

van Veluw SJ, Shih AY, Smith EE, Chen C, Schneider JA, Wardlaw JM, Greenberg SM, and Biessels GJ (2017). Detection, risk factors, and functional consequences of cerebral microinfarcts. Lancet Neurol 16, 730–740. [PubMed: 28716371]

Vanderkooi JM, Maniara G, Green TJ, and Wilson DF (1987). An optical method for measurement of dioxygen concentration based on quenching of phosphorescence. J. Biol. Chem 262, 5476–5482. [PubMed: 3571219]

Vinogradov SA (2005). Arylamide dendrimers with flexible linkers via haloacyl halide method. Organic Letters 7, 1761–1764. [PubMed: 15844900]

Vinogradov SA, and Wilson DF (2012). Porphyrin-dendrimers as biological oxygen sensors In Designing Dendrimers Capagna S, and Ceroni P, eds. (New York: Wiley).

Weber B, Keller AL, Reichold J, and Logothetis NK (2008). The microvascular system of the striate and extrastriate visual cortex of the macaque. Cerebral Cortex 18, 2318–2330. [PubMed: 18222935]

Wilson DF (2015). Programming and regulation of metabolic homeostasis. Am J. Physiol 308, E506–E517.

Yoshihara T, Hirakawa Y, Hosaka M, Nangaku M, and Tobita S (2017). Oxygen imaging of living cells and tissues using luminescent molecular probes. J. Photochem. Photobio. C - Photochem. Rev 30, 71–95.

HIGHLIGHTS

- A high-performance phosphorescent probe for measuring oxygen in biological systems
- Two-photon imaging as deep as 600μm at ~60 times higher speed than existing methods
- A probe delivery approach that avoids local tissue damage in the brain
- The ability to perform longitudinal oxygen imaging over many days and periods

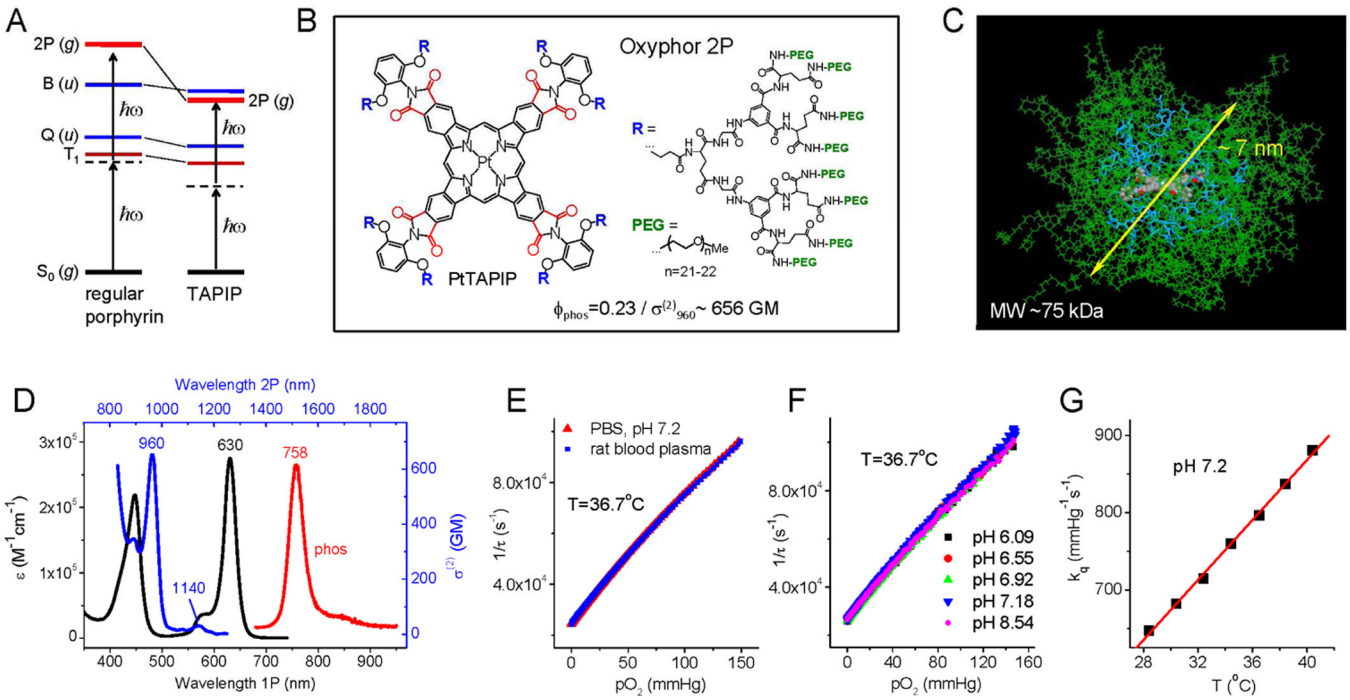

Figure 1.

Structure and properties of Oxyphor 2P. (A) Energy diagram showing low-lying electronic *ungerade* states (*u*-states), Q and B (Soret), in regular porphyrins (left) and in tetraarylphthalimidoporphyrins (TAPIP, right). In TAPIP a 2P-active *grade* state (*g*-state) is stabilized below the B state level, allowing for efficient 2P-excitation without overlapping with low vibronic sublevels of the triplet state (T_1). (B) Structure of probe Oxyphor 2P, which is composed of PtTAPIP core, mixed glutamate/aryl-glycine dendrons and multiple peripheral PEG groups (see Supplemental Information for synthesis and characterization). In PtTAPIP, eight carbonyl groups (shown in red) are locked in plane with the porphyrin, ensuring high degree of conjugation with the macrocycle and maximal stabilization of the *g*-state. (C) Calculated structure (molecular mechanics, AMBER force field) of the probe molecule in water (modeled as dielectric continuum): core porphyrin (colored by atom), dendritic branches (blue), PEG chains (green). The average diameter of the semi-globular molecule is ~7 nm. (D) 1P (black) and 2P (blue) absorption and phosphorescence emission (red) spectra of Oxyphor 2P in water. The 2PA spectrum shows two maxima: 960 nm (656 GM) and 1140 nm (30 GM). (E) Stern-Volmer oxygen quenching plots of Oxyphor 2P in phosphate buffered saline (pH 7.1) and in rat blood plasma (T=36.7°C). (F) Stern-Volmer oxygen quenching plots of the probe at different pH levels. (G) The quenching plots (pO_2 *vs* τ) were fit to a modified Stern-Volmer equation, $pO_2(\tau)=1/(a\times k_q\times\tau^p)+1/(k_q\times\tau_0)$, where τ_0=38 μs (phosphorescence lifetime in the absence of oxygen) and empirical parameters a=14.8 and p=−1.26 are constants, while the oxygen quenching constant k_q changes linearly with temperature (Supplemental Information).

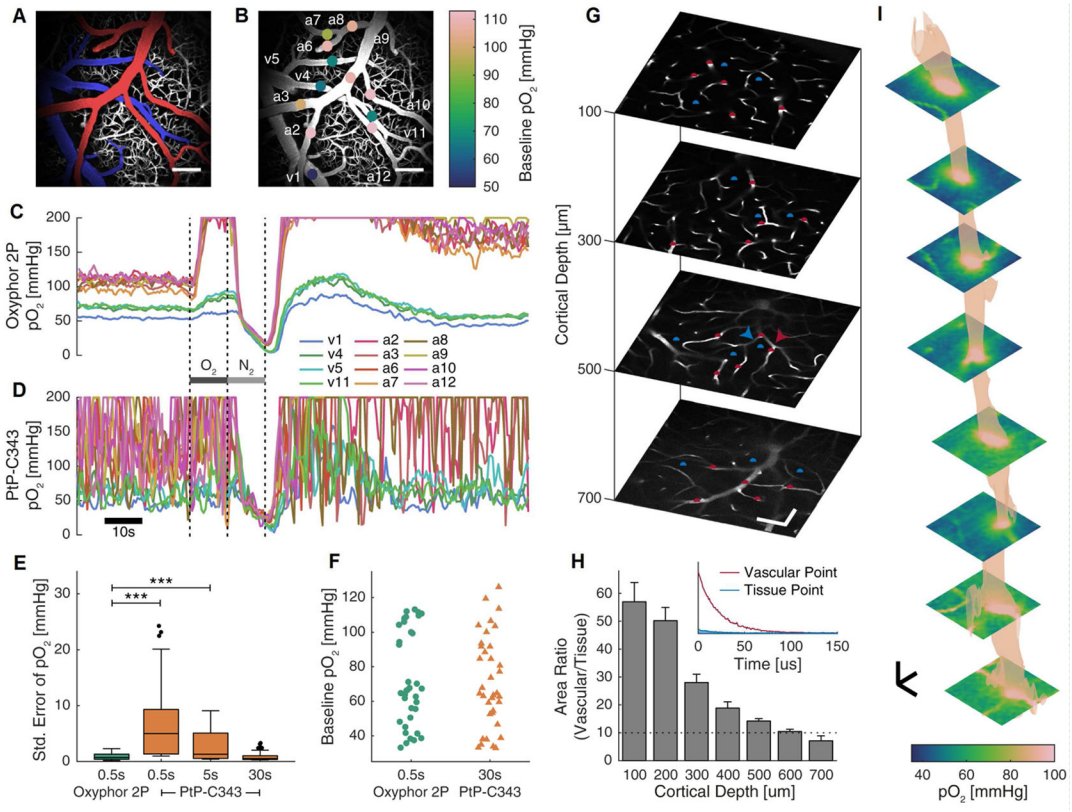

Figure 2.

Oxyphor 2P offers ~60 fold improvement in the temporal resolution over the previous probe PtP-C343 (Finikova et al., 2008) and allows imaging up to 600µm below the cortical surface in vasculature and tissue. (A) Maximum intensity projection of a 250µm-thick image stack of the cortical vasculature labeled with FITC-dextran and colored to highlight the major arterial (red) and venous (blue) branches, in a freely-breathing, lightly sedated mouse. Scale bar, 100µm. (B) The locations of the 12 points used in a mouse for pO_2 measurements in c-d, color-coded to display the respective baseline pO_2 values. The labels identify whether the vessel is an arterial (a) or venous (v) location. (C-D) Temporal profiles of pO_2 values at the points labeled in b, in response to changes in the inspired gas from air to 100% O_2 (dark grey bar) then 100% N_2 (light grey bar). (E) Summary quantification of the average standard error in the pO_2 measurements (example shown in C-D) during the baseline period, corresponding to different data acquisition times: 0.5s (150 phosphorescence decays averaged per location); 5s (1500 decays); 30s (9000 decays). See STAR Methods for data acquisition protocol. *** represents $p < 0.001$, linear mixed effects models. N = 36 locations in 3 mice. (F) Baseline pO_2 when measured with Oxyphor 2P and PtP-C343 ($p=0.72$, linear mixed effects models). (G) Images of the FITC-dextran labeled microvasculature at increasing cortical depth, overlaid with measurement locations for phosphorescence decays in vessels (red) and the tissue (blue). Arrowheads indicate the points plotted in the inset in h. Scale bars, 50µm. (H) Main panel: Summary quantification of the ratio of area under the phosphorescence decay curves in the vasculature *vs* tissue. The dashed line (Area Ratio=10) indicates the threshold above which >91% of the detected photons originate in the focal point. Error bars represent s.e.m. N = 148 points from 7 regions across 3 mice. Inset:

Phosphorescence decays measured at the points in (G) marked by arrowheads. Although Oxyphor 2P is not present in the parenchyma, some phosphorescence is detected, increasing with depth, which can confound localized measurements. (I) Selected images (separated by 75μm, interpolated for display purposes) and a 90mmHg isosurface derived from a high-resolution volumetric image stack measuring pO_2 simultaneously in blood and tissue. Oxyphor 2P was injected into the cisterna magna in a minimally invasive manner and reached the tissue in the imaging region with the CSF (see main text and Supplemental Information). pO_2 measurement image grids were recorded every 25μm in *z* from 0–600μm below the cortical surface. Scale bars: 25μm.

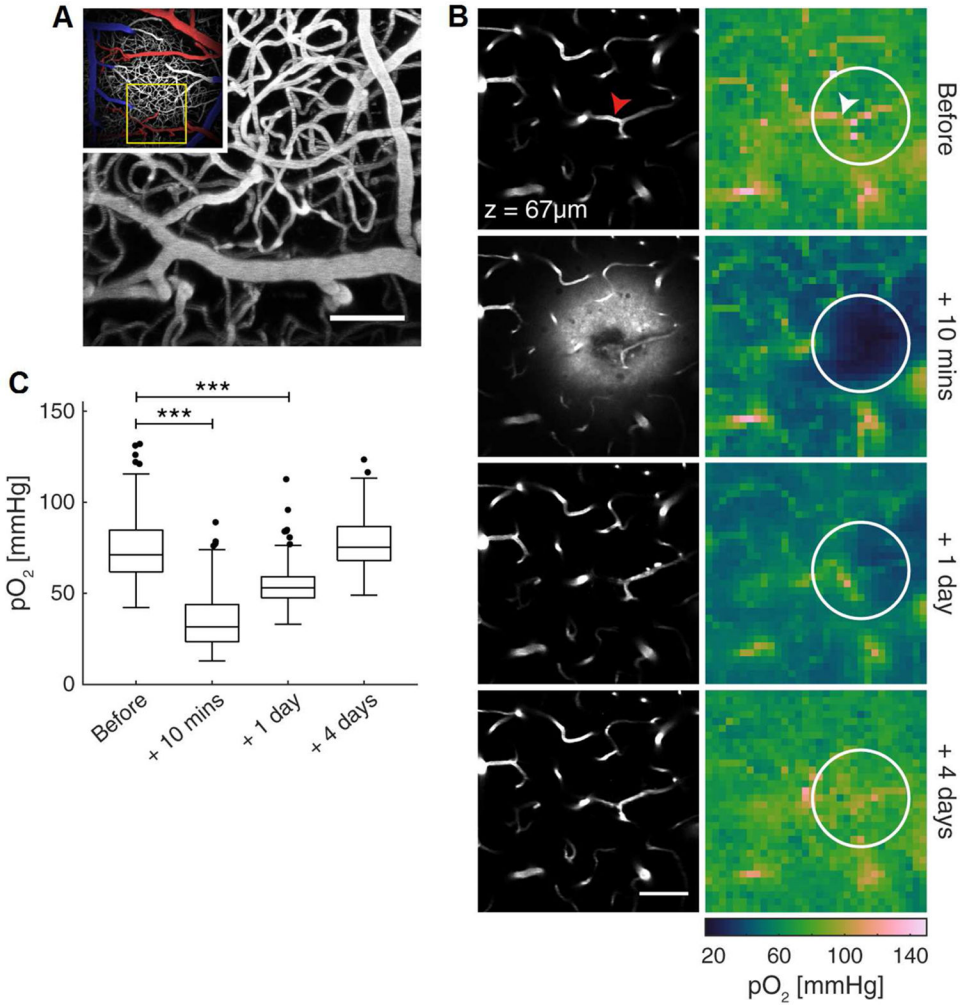

Figure 3.

Oxyphor 2P enables longitudinal non-invasive imaging of extravascular pO_2 following localized micro-stroke. (A) Main image: maximum intensity projection of a ~200 μm-thick image stack of the cortical vasculature labeled with FITC-dextran in a freely-breathing anesthetized mouse. Inset: a wider view of the surrounding region, colored to highlight the major arterial (red) and venous (blue) branches. (B) Left column: images of the microvasculature 67 μm below the cortical surface before (top) and at three time points after inducing a localized hemorrhagic stroke. The fluorescent plasma label is visible in the tissue immediately following the stroke. Right column: images of pO_2 at the same time points as the corresponding anatomical images to the left. The arrowheads indicate the location within the blood vessel where the laser was focused to induce the stroke. The circle indicates the region used for quantifying pO_2 in panel (C). (C). Summary quantification of the pO_2 values at each time point in the stroke-affected regions (example region circled in (B)). *** represents $p < 0.001$, linear mixed effects models. Only comparisons with values before the stroke are shown. N=290 points from 4 strokes across 4 mice. As per Figure 2, Oxyphor 2P was injected into the *cisterna magna* and reached the tissue in the imaging region *via* diffusion with the CSF (see main text and Supplemental Information). After the initial

injection the concentration of Oxyphor 2P was sufficient for tissue imaging at all time points (day of injection, 1 day after injection, 4 days after injection). All scale bars: 50 μm.

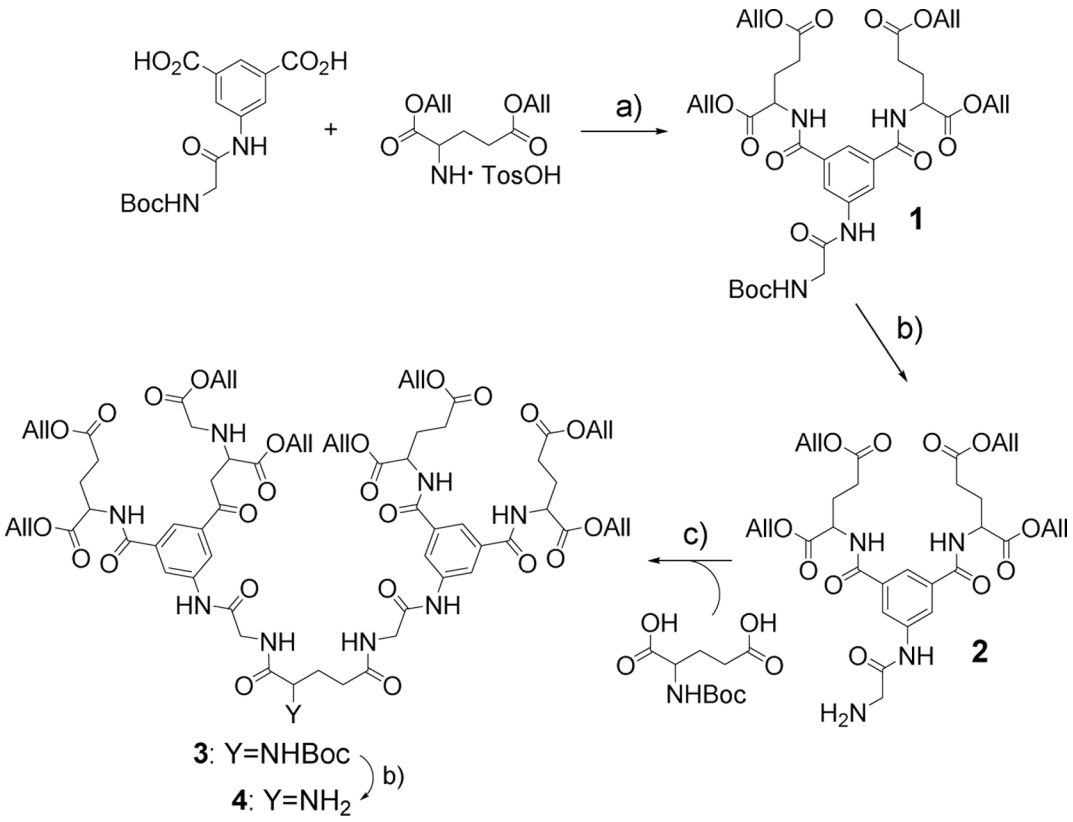

Scheme 1.

Synthesis of dendrons. Reagents and conditions: (a) CDMT, N-methylmorpholine, DMF, r.t., 48 h (82%); (b) TFA/THF~2:1, r.t., 12 h (85%); (c) HBTU, DIPEA, DMF, r.t., 48 h (75%).

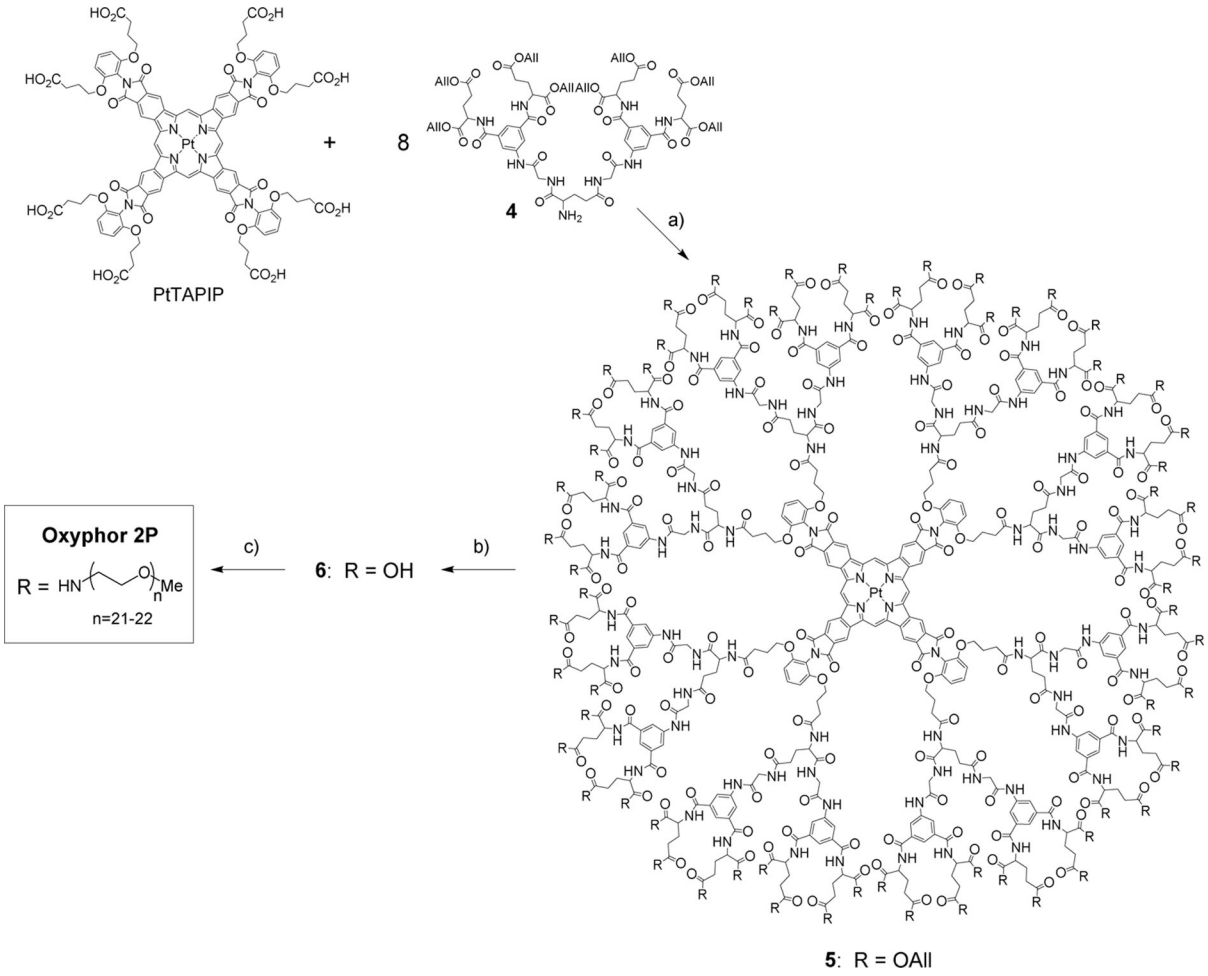

Scheme 2.

Synthesis of Oxyphor 2P. Reagents and conditions: (a) HBTU, DIPEA, DMF, r.t., 48–72 h (90–95%); (b) Pd(PPh3)4, morpholine, DMF, r.t., 48 h (90–95%); (c) NH2-PEG (Av. MW~1000), HBTU, DIPEA, DMF, r.t., 120–168 h (80–90%).